SUPPLEMENTARY INFORMATION

Hexagonal Boron Nitride for Sulfur Corrosion Inhibition

Govind Chilkoor[1,2], Kalimuthu Jawaharraj[1], Bhuvan Vemuri[1], Alex Kutana[3], Manoj Tripathi[4], Divya Kota[5], Taib Arif[6], Tobin Filleter[6], Alan B. Dalton[4], Boris I. Yakobson[3], M. Meyyappan[7], Muhammad M. Rahman[3*], Pulickel M. Ajayan[3*], Venkataramana Gadhamshetty[1,2*]

[1]Department of Civil and Environmental Engineering, South Dakota School of Mines and Technology, SD 57701, United States
[2]2-Dimensional Materials for Biofilm Engineering Science and Technology (2DBEST) Center, South Dakota School of Mines and Technology, SD 57701, United States
[3]Department of Materials Science and NanoEngineering, Rice University, TX 77005, United States
[4]Department of Physics and Astronomy, University of Sussex, Brighton BN1 9RH, United Kingdom
[5]Department of Nanoscience and Nanoengineering, South Dakota School of Mines and Technology, SD 57701, United States
[6]Department of Mechanical and Industrial Engineering, University of Toronto, Ontario M5S 3G8, Canada
[7]Center for Nanotechnology, NASA Ames Research Center, CA 94035, United States

Corresponds to: mr64@rice.edu, ajayan@rice.edu, Venkata.Gadhamshetty@sdsmt.edu

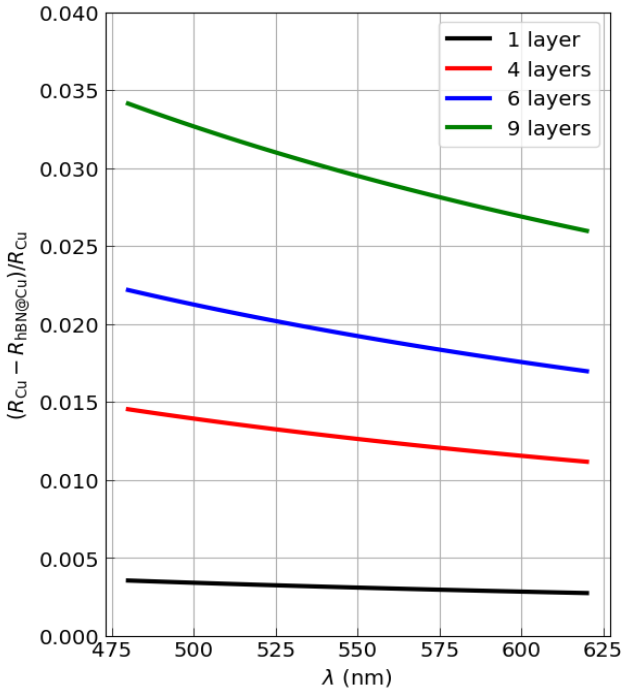

Figure S1. Optical contrast of atomic hBN layers on Cu

Optical contrast of few-layer hBN on Cu was calculated according to $(R_{Cu}–R_{hBN@Cu})/R_{Cu}$ and is shown in **Figure S1**. Here, R_{Cu} is the reflectance of bare Cu, and $R_{hBN@Cu}$ is the reflectance of few-layer hBN on Cu. The reflectance was calculated using the transfer matrix method.[S1] Refractive index of hBN was taken to be 1.85 at 560 nm, 1.91 at 480 nm, and 1.80 at 640 nm,[S2] and linearly interpolated at other wavelengths, while the wavelength-dependent complex refractive index of copper was taken from a reference handbook.[S3] It follows that hBN on Cu is highly optically transparent, decreasing the optical reflectivity of Cu at 550 nm from 60.2% to 60.0%, 59.4%, and 58.4% for 1, 4, and 9 layers of hBN, respectively.

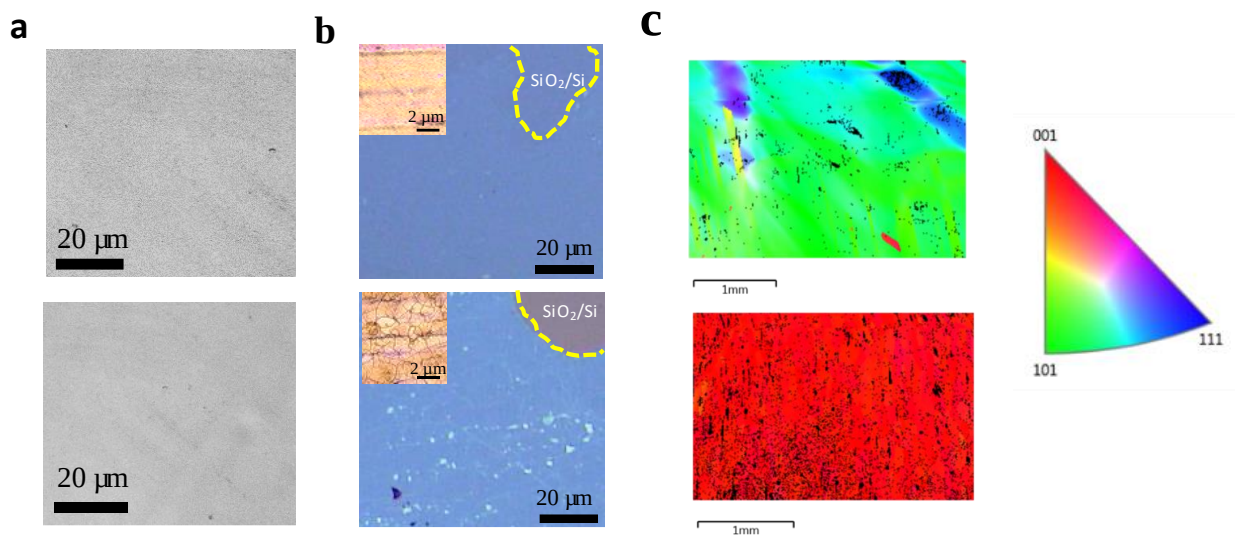

Figure S2. (a) SEM image of pristine FL-hBN-Cu (upper panel) and ML-hBN-Cu (lower panel). (b) Optical images of FL- hBN (upper panel) and (b) ML-hBN on copper foil transferred on SiO_2. Inset shows the pristine Cu foil with corresponding hBN coating. (c) EBSD orientation maps of FL-hBN-Cu (upper panel) and ML-hBN-Cu (lower panel) showing predominant mono crystalline Cu (101) and Cu (001) for FL-hBN-Cu and ML-hBN-Cu, respectively. The image at right shows the corresponding inverse pole figure. The grains marked in red, blue, and green are along (001), (111) and (101) respectively.

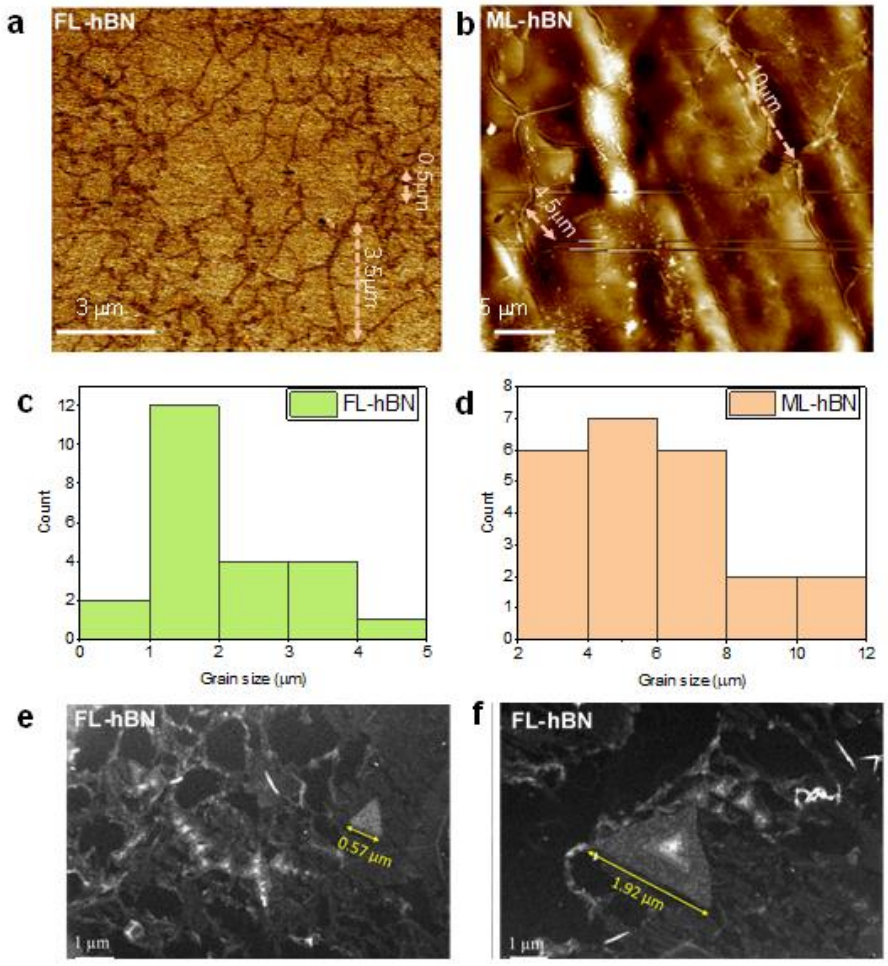

Figure S3. Grain size and shape analysis in hBN layers. (a) AFM topographical image of FL-hBN along with force-distance spectroscopy. Dark contour lines illustrate grain boundaries (GBs). Dashed arrows show grain dimensions along major and minor axis. (b) AFM topography of ML-hBN. (c) and (d) A histogram showing the size distribution of FL-hBN and ML-hBN grains, respectively. (e) and (f) TEM dark field images of FL-hBN showing triangular crystals with a length of 0.57 μm and 1.92 μm, respectively.

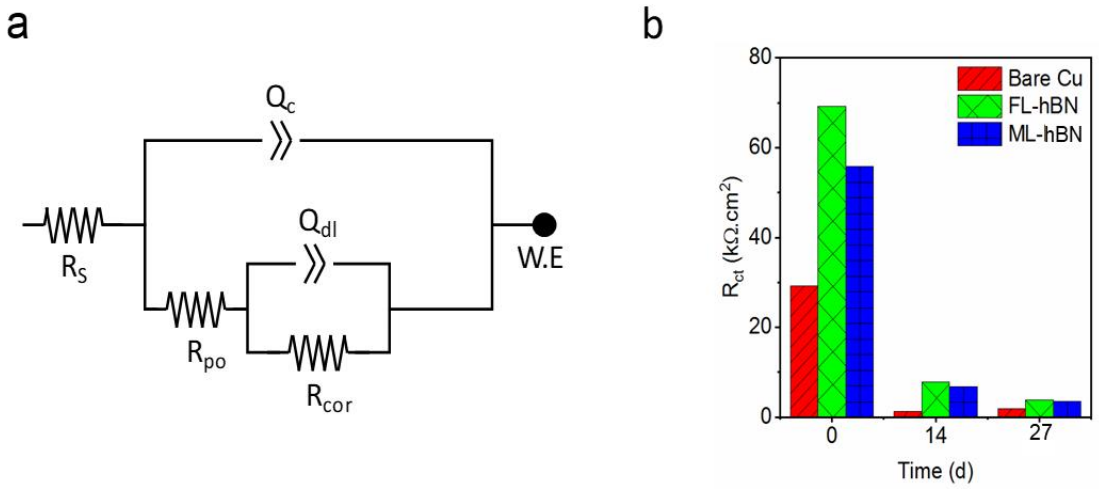

Figure S4. (a) Electrical equivalent circuit used to fit Nyquist plots obtained for both abiotic and biotic sulfur compound corrosion. (b) Temporal variation of charge transfer resistance of bare Cu, FL-hBN-Cu and ML-hBN-Cu in biogenic sulfur environments

Description of electrical equivalent circuit to fit abiotic and biotic Bode impedance plot

Bode plot for all samples were fitted to an electrical equivalent circuit (EEC) with two-time constants (Fig. S4a). The $R_{po}Q_c$ circuit represents pore resistance (R_{po}) and constant phase element representing the coating capacitance (Q_c) and corresponds to coating/solution interface in the case of hBN coated Cu. For bare Cu, $R_{po}Q_c$ circuit represents the pore resistance and capacitance offered by the temporary copper oxide film. The R_{cor} Q_{dl} represents the corrosion resistance (R_{cor}) and constant phase elements representing the double layer capacitance (Q_{dl}) of underlying copper surfaces and describes the corrosion process at solution/substrate interface. The total corrosion resistance (R_{cor}) is calculated taking the sum of R_{po} and $R_{cor.}$ The value of constant phase element capacitance (Q) was converted into capacitance (C) by using its corresponding resistance (R) value using the below equation (1)

$$C = R^{\left(\frac{1-n}{n}\right)} \; Q^{\frac{1}{n}} \qquad (1)$$

where n is the exponent in the constant phase element

Corrosion resistance against biotic sulfur medium

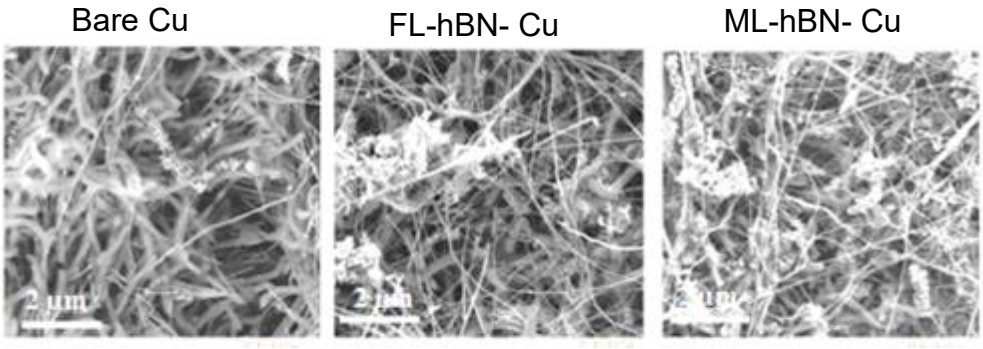

Figure S5. SEM images at higher magnification of bare cu, FL-hBN-Cu and ML-hBN-Cu after 27 days of exposure. The SEM analysis suggest that hBN coatings do not impede biofilm formation during longer exposure

AFM analysis of surface roughness of hBN coated Cu

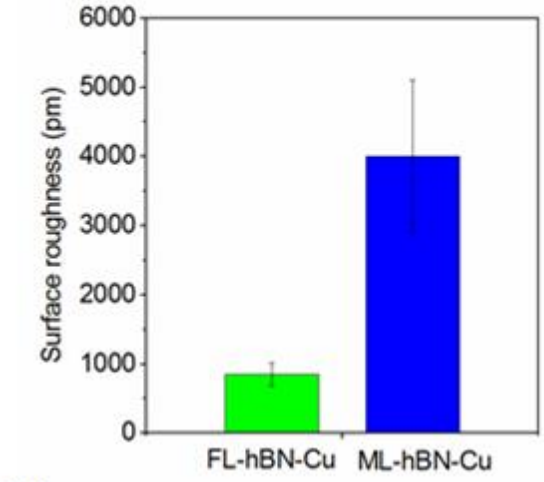

Figure S6. Root mean square (RMS) surface roughness obtained from AFM analysis of FL-hBN-Cu and ML-hBN-Cu coating over the 500nm region.

KPFM characterization. The KPFM characterization was carried out using an AFM-Bruker Dimension Icon. To minimize the ambient noise and vibrations, an insulated box mounted over an anti-vibrant stage was used to contain the samples. We collected the topography and surface potential maps in a single acquisition using a Peak-force (PF) operation mode in two pass modes. During the first pass of the line scanning, the tip was softly tapped (<1 nN) onto the sample to gather the topographical data. In the second pass over the same scanning line, the cantilever was lifted 10 nm away from the surface to determine the contact potential difference (CPD, V). For the KPFM measurement, a PFQNE-AL probe consisting of a metal-coated soft silicon–nitride tip with 5 nm nominal diameter, 300 ± 100 kHz resonant frequency, and 0.8 ± 0.2 N/m spring constant was used. It was optimized for electrical modes with a proprietary reflective coating on the backside. To verify the consistency of resonance frequency and stiffness of the cantilever, we performed thermal tune calibration before each imaging session. We used freshly cleaved graphite (HOPG, WF = 4.66 eV) to measure the WF of tip using the following relation. This relation was used to measure the WF of the sample:

$$WF_{sample} = WF_{tip} - eV_{dc} \quad (2)$$

Also, we measured the contact potential difference (CPD, mV) at the grain and GBs in the specified regions as identified in Figure S7 and converted them into work function (WF, eV) using the following relationship. The CPD and WF were determined for both the pristine and exposed regions of the grains and GBs.

$$e(CPD) = \varphi_{sample} - \varphi_{tip} \quad (3)$$

where, e = electronic charge, φ_{sample} = work function of sample, φ_{tip} = work function of AFM tip used for investigation.

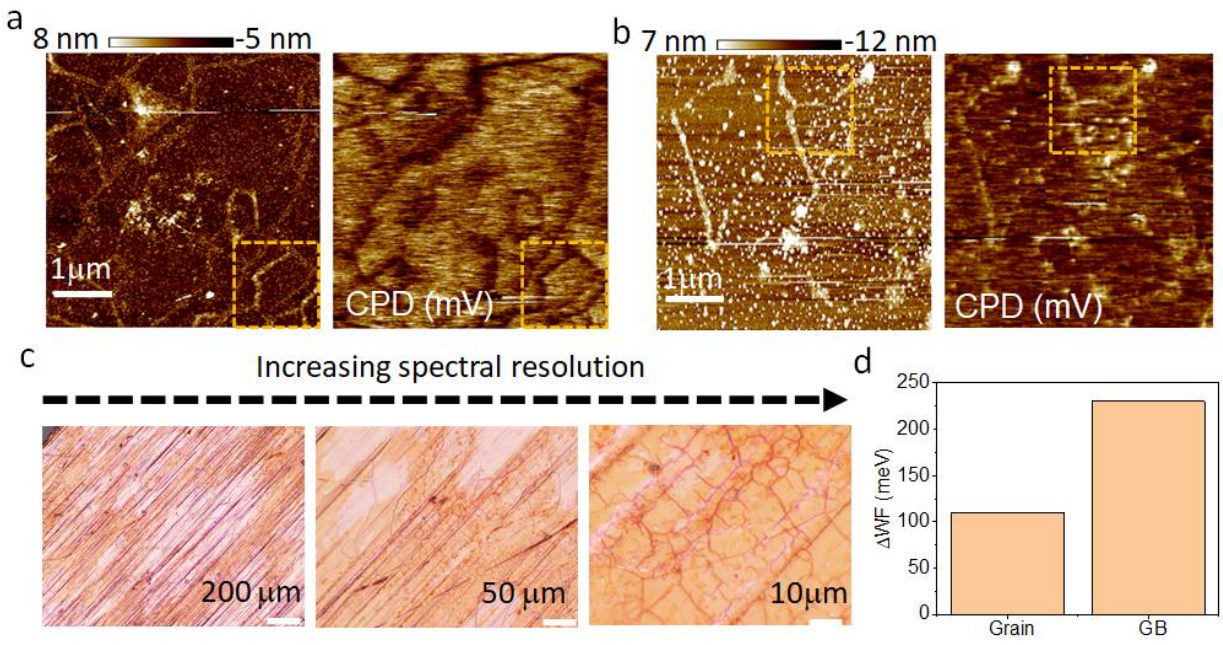

Figure S7. Morphology and surface potential map of (a) pristine FL-hBN/Si-SiO_2. (b) FL-hBN/ Si-SiO_2 exposed to 1M H_2SO_4 showing the hBN of heavily decorated with SO_4^{2-} salts. (c) Optical images of ML-hBN on Cu surface of different optical resolution of 5X, 20X and 100X . (d) ΔWF at grain *vs.* GB exposed to the corrodent.

Details of DFT Simulations. We have studied the effect of double vacancy defects on the local work function near the hBN layers as a model for the point defects. The electrostatic potential distribution was calculated near the hBN double vacancy with and without the adsorbed sulfide radical (HS•) (Figure 6). The local work function was determined by adding the local potential near the vacancy to the calculated work function of pristine hBN on Cu. The WF along the horizontal and vertical lines 3 Å above the hBN plane, as marked by dotted lines in Figures 6e is shown in Figures 6f and 6g, respectively. The double vacancy yielded an electric dipole, creating a negatively charged pair of nitrogen and positively charged pair of boron. The vacancy dipole field extends over distances of the order of vacancy size. The field displayed an amplitude of ~200 meV at 3 Å above the plane. HS radical additionally perturbed the electric field with positive H and negative S. Figures 6i, j show the potential for HS above a double vacancy along the horizontal

and vertical cuts at a distance of 5.5 Å above hBN, marked in Figure 6h, revealing a local field with an amplitude of ~400 meV. Thus, in the former case of double vacancy the potential increases, increasing the local WF, while in the latter case of double vacancy with HS•, the potential (work function) decreases. Thus, the decreased WF creates an additional support for electron removal, which may increase the oxidation reaction at that location and promote corrosion.

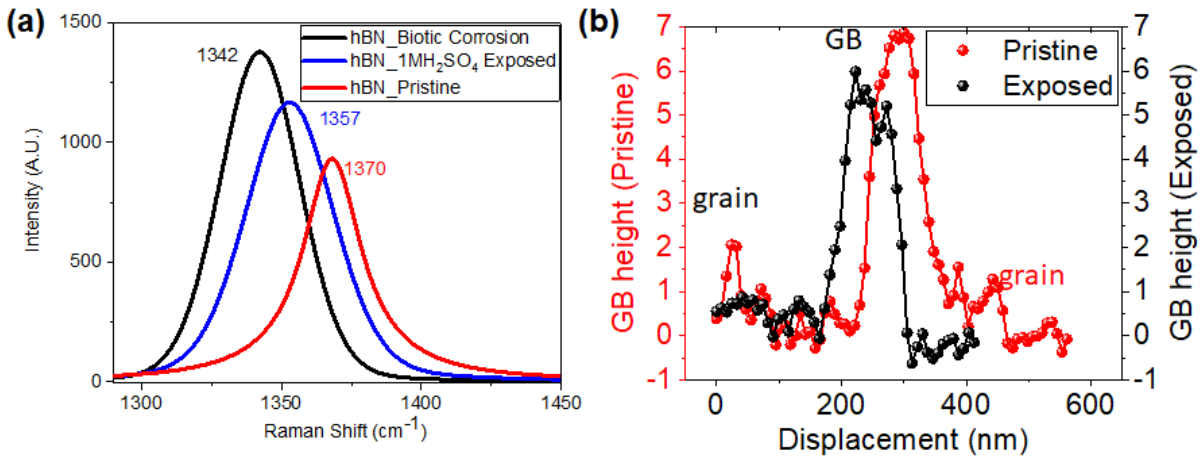

Figure S8. (a) "Post-mortem" study of atomic ML-hBN layers exposed to corrosive environments. Raman spectrum range between 1250-1450 cm^{-1} for the pristine hBN and hBN samples exposed to biotic and abiotic corrosion environments. The presence of the hBN E_{2g} Raman modes reveals the retention of hBN layer, though its red shift indicates different extent of strain and doping in biotic and abiotic environments. (b) Topographic line profile over grain-GB-grain region of pristine and exposed hBN. The height of the GB is similar around 6.5 nm before and after the exposure of corrodent.

Table S1. The electrochemical parameters determined from potentiodynamic polarization for bare Cu, FL-hBN-Cu and ML-hBN-Cu exposed to 0.5 M H_2SO_4 medium

Sample	β_a (mV/dec)	β_c (mV/dec)	i_{corr} ($\mu A\ cm^{-2}$)	E_{corr} (mV)	Corrosion rate (mpy)	Corrosion protection efficiency (%)
Bare Cu	47	79	1060	76.30	484.4	-
FL-hBN-Cu	13	23	77.20	51.20	35.25	93
ML-hBN-Cu	59	54	73.8	370	33.72	93

Table S2. EEC parameters for bare Cu, FL-hBN-Cu and ML-hBN-Cu in 0.5M H_2SO_4 solution

Sample	R_{soln} ($\Omega.cm^2$)	R_{cor} ($\Omega.cm^2$)	R_{po} ($\Omega.cm^2$)	R_{corr} ($R_{cor} + R_{po}$) ($K\Omega.cm^2$)	C_{dl} ($\mu F/cm^2$)	C_c ($\mu F/cm^2$)
Bare-Cu	1.25	86.1	2.4	0.0891	255	5.71
FL-hBN-Cu	0.61	460	82.2	0.542	108	50
ML-hBN-Cu	1.42	1070	130	1.19	37	44

Table S3. The electrochemical parameters determined from potentiodynamic polarization for bare MS, FL-hBN-Cu and ML-hBN-Cu in 0.5 M Na_2S medium

Sample	β_a (mV/dec)	β_c (mV/dec)	i_{corr} ($\mu A\ cm^{-2}$)	E_{corr} (mV)	Corrosion rate (mpy)	Corrosion protection efficiency (%)
Bare Cu	148	730	7.7	85.20	3.525	-
FL-hBN-Cu	76	123	0.451	-71.20	0.205	94
ML-hBN-Cu	79	207	0.643	66.20	0.293	94

Table S4. EEC parameters for bare Cu, FL-hBN-Cu and ML-hBN-Cu in 0.5 M Na_2S solution

Sample	R_{soln} ($\Omega.cm^2$)	R_{cor} ($\Omega.cm^2$)	R_{po} ($\Omega.cm^2$)	R_{corr} ($R_{cor}+R_{po}$) ($K\Omega.cm^2$)	C_{dl} ($\mu F/cm^2$)	C_c ($\mu F/cm^2$)
Bare-Cu	795	29770	3050	32.8	148	40.5
FL-hBN-Cu	905.5	1.61×10^5	1.13×10^5	274	517	6.0
ML-hBN-Cu	962	4.63×10^4	2.97×10^4	75.9	773	5.8

Table S5. EEC parameters for bare Cu, FL-hBN-Cu and ML-hBN-Cu in planktonic *D. alaskensis*

Sample	R_{soln} ($\Omega.cm^2$)	R_{cor} ($\Omega.cm^2$)	R_{po} ($\Omega.cm^2$)	R_{corr} ($R_{cor} + R_{po}$) ($K\Omega.cm^2$)	C_{dl} ($\mu F/cm^2$)	C_c ($\mu F/cm^2$)
Bare-Cu	45.29	7.96×10^4	5.04×10^4	79.6	-	-
FL-hBN-Cu	35.08	6.92×10^4	5.45×10^4	123.6	30.8	111.2
ML-hBN-Cu	38.07	5.58×10^4	8.96×10^4	145.4	159.7	222.6

Table S6. EEC parameters for bare Cu, FL-hBN-Cu and ML-hBN-Cu on day 14 in *D. alaskensis* cells

Sample	R_{soln} ($\Omega.cm^2$)	R_{cor} ($\Omega.cm^2$)	R_{po} ($\Omega.cm^2$)	R_{corr} ($R_{cor} + R_{po}$) ($K\Omega.cm^2$)	C_{dl} ($\mu F/cm^2$)	C_c ($\mu F/cm^2$)
Bare-Cu	41.4	1.23×10^3	9.61×10^1	1.3	-	-
FL-hBN-Cu	39.6	7.88×10^3	2.85×10^3	10.7	26.54	504.9
ML-hBN-Cu	37.0	6.83×10^3	1.65×10^3	8.48	68.77	426.7

Table S7. EEC parameters for bare Cu, FL-hBN-Cu and ML-hBN-Cu on day 27 in *D. alaskensis* cells

Sample	R_{soln} ($\Omega.cm^2$)	R_{ct} ($\Omega.cm^2$)	R_{po} ($\Omega.cm^2$)	R_{corr} ($R_{Cor} + R_{po}$) ($K\Omega.cm^2$)	C_{dl} ($\mu F/cm^2$)	C_c ($\mu F/cm^2$)
Bare-Cu	29.1	1.82×10^3	9.96×10^2	2.8	-	-
FL-hBN-Cu	38.5	3.82×10^3	1.63×10^3	5.4	107.8	1164
ML-hBN-Cu	39.1	3.47×10^3	2.92×10^2	3.8	489.4	398.3

References

(S1) Gupta, S.; Shirodkar, S. N.; Kutana, A.; Yakobson, B. I. In Pursuit of 2D Materials for Maximum Optical Response. *ACS Nano* **2018**, *12* (11), 10880–10889. https://doi.org/10.1021/acsnano.8b03754.

(S2) Golla, D.; Chattrakun, K.; Watanabe, K.; Taniguchi, T.; LeRoy, B. J.; Sandhu, A. Optical Thickness Determination of Hexagonal Boron Nitride Flakes. *Appl. Phys. Lett.* **2013**, *102* (16), 161906. https://doi.org/10.1063/1.4803041.

(S3) Lynch, D. W.; Hunter, W. R. - Comments on the Optical Constants of Metals and an Introduction to the Data for Several Metals. In *Handbook of Optical Constants of Solids*; Palik, E. D., Ed.; Academic Press: Burlington, **1997.** 275–367. https://doi.org/10.1016/B978-012544415-6.50015-7.